



Highly selective production of singlet oxygen by manipulating the spin state of single-atom Co–N moieties and electron localization

Zhiwei Wang^a, Yu Wang^a, Wenlong Wang^a, Dexiu Wu^a, Qianyuan Wu^{a,*}, Hongying Hu^{a,b}

^a Key Laboratory of Microorganism Application and Risk Control of Shenzhen, Guangdong Provincial Engineering Research Center for Urban Water Recycling and Environmental Safety, Institute of Environment and Ecology, Tsinghua-Berkeley Shenzhen Institute, Tsinghua Shenzhen International Graduate School, Tsinghua University, Shenzhen 518055, PR China

^b Environmental Simulation and Pollution Control State Key Joint Laboratory, Beijing Laboratory for Environmental Frontier Technologies, School of Environment, Tsinghua University, Beijing 100084, PR China

ARTICLE INFO

Keywords:

Single-atom catalyst
Peroxymonosulfate
Singlet oxygen
Selective conversion
Endocrine disrupting chemicals

ABSTRACT

Singlet oxygen ($^1\text{O}_2$) is a reactive species with oxidation selectivity that is preferred in advanced oxidation processes. However, the underlying mechanism of $^1\text{O}_2$ selective production remain ambiguous. In this study, we demonstrated that electron localization and high spin state of metal active sites favored peroxymonosulfate (PMS) co-adsorption and dissociation, which promoted selective production of $^1\text{O}_2$. Under theoretical guidance, single Co atoms anchored on uneven graphite carbon nitride nanosheet (Co-SA/CMN) was fabricated and exhibited the highest $^1\text{O}_2$ production selectivity so far with 87.8% of the PMS consumed was converted to $^1\text{O}_2$. The Co-SA/CMN/PMS system exhibited remarkable degradation efficiency to multiple organic pollutants, show strong resistance to environmental interference and robust stability at the device level. Co-SA/CMN/PMS oxidation was assessed as a safe and detoxifying technology, the estrogenic activity and toxicity originating from 17 β -estradiol (E2) or its degradation by-products were sufficiently removed. These findings deepen the mechanistic understanding of the origins of high $^1\text{O}_2$ production selectivity and provide a rational strategy for precisely controlling $^1\text{O}_2$ generation in PMS activation.

1. Introduction

Singlet oxygen ($^1\text{O}_2$) as a nonradical derivative of O_2 is considered as the most useful reactive oxygen species (ROS) [1,2] and plays a crucial part in chemical, biomedical and environmental fields [3–5]. $^1\text{O}_2$ ($^1\Delta_g$) is 94 kJ/mol (ΔG_{298}^0) above the ground state triplet oxygen (O_2 ($^3\Sigma_g^-$)), which makes $^1\text{O}_2$ one of the most reactive ROS [6,7]. Comparing with hydroxyl/sulfate radicals, $^1\text{O}_2$ has the unique properties of longer lifetime, higher selectivity and better safety which makes it show great application prospect for practical wastewater purification. The lifetime of $^1\text{O}_2$ in water is about 4–6 μs which is much longer than the ultrashort-lived hydroxyl/sulfate radicals. The relatively long lifetime and fast movement brings $^1\text{O}_2$ of 0.3 μm diffusion distance which is enough for the sufficient mass transfer with pollutants [8]. In addition, $^1\text{O}_2$ has an unoccupied π^* orbital, which endows it with high electrophilicity and selectivity toward electron-rich substances [9,10], such as aromatic organic pollutants [11,12] and unsaturated biomolecules

including pathogenic microorganisms [13]. Due to its oxidation selectivity, it has been reported that $^1\text{O}_2$ is less likely to be affected by aqueous organic matter in natural waters, be inert to the inorganic ions and have a wide pH tolerance. Therefore, $^1\text{O}_2$ could enable the rapid and accurate oxidation of high-priority pollutants such as EDCs, antibiotics, and pharmaceuticals in low concentration and with almost no interference by the actual wastewater matrix [5,14,15]. Actually, the anti-interference and selective features are urgently needed in practical wastewater treatment process. Meanwhile, unlike hydroxyl/sulfate radicals have the risk of disinfection by-products formation, $^1\text{O}_2$ has long been considered as a green oxidant that does not produce any known hazardous byproducts due to its oxidation selectivity and mild oxidation capacity [16,17]. By virtue of the unique properties, $^1\text{O}_2$ is also extensively used in medical applications (e.g., selective oxidation of proteins in tumor cells) and green organic synthesis, which involve even more complex matrix [18,19].

H_2O_2 activation to produce $^1\text{O}_2$ is commonly used but the yield is

* Correspondence to: Division of Energy and Environment, Tsinghua Shenzhen International Graduate School, Tsinghua University, Room 1810, Shenzhen 518055, PR China.

E-mail addresses: wu.qianyuan@sz.tsinghua.edu.cn, wuqianyuan@tsinghua.edu.cn (Q. Wu).

<https://doi.org/10.1016/j.apcatb.2022.122248>

Received 8 September 2022; Received in revised form 15 October 2022; Accepted 30 November 2022

Available online 2 December 2022

0926-3373/© 2022 Elsevier B.V. All rights reserved.

lowered by the Haber–Weiss reaction ($\text{O}_2^{\bullet-} + \text{H}_2\text{O}_2 \rightarrow \bullet\text{OH} + \text{OH}^- + \text{O}_2$) [20]. Recently, many researchers have researched on the activation of persulfate, including peroxymonosulfate (PMS, HSO_5^-) and peroxydisulfate (PDS, $\text{S}_2\text{O}_8^{2-}$), by heterogeneous catalysts to produce $^1\text{O}_2$, which could avoid competition reaction and work to the advantage of heterogeneous catalysts. However, heterogeneous persulfate catalysts are preferred to generate diverse reactive species such as $\bullet\text{OH}$ and $\text{SO}_4^{\bullet-}$ [21], which would decrease the ratio of persulfate converted to $^1\text{O}_2$. There is an urgent need to illustrate the key steps and controlling factors of $^1\text{O}_2$ generation and regulate PMS to selectively convert into $^1\text{O}_2$.

Because of insufficient understanding of the formation mechanism, there are few heterogeneous catalysts that have achieved high $^1\text{O}_2$ production selectivity. A type of heterogeneous catalyst with atomically dispersion of metal, termed as single-atom catalysts (SACs), has been used to achieve high $^1\text{O}_2$ selectivity owing to the utmost metal utilization, coordination-unsaturated active center and highly uniform active metal center. For example, single-atom $\text{Co}_{\text{N}_{2+2}}$ sites were reported to achieve almost 100% PMS conversion to $^1\text{O}_2$ and weak positive Co atoms could prevent spontaneous dissociation of adsorbed PMS and facilitate $^1\text{O}_2$ generation [22]. However, the $^1\text{O}_2$ generation selectivity mentioned here is the proportion of $^1\text{O}_2$ concentration in the generated ROS. There is no mention of quantitative methods for various ROS in this research. As for the radicals with a short lifetime such as $\bullet\text{OH}$ and $\text{SO}_4^{\bullet-}$, most of the quantitative methods have difficulty in achieving accurate determination of radicals' concentrations, which are often lower than the actual value. The lower concentrations of other radicals highlight the high proportion of $^1\text{O}_2$. Zhang et al. developed a graphite carbon nitride-supported Fe single-atom catalyst (Fe_1/CN), which tended to adsorb the terminal O of PMS to promote formation of $\text{SO}_5^{\bullet-}$ by PMS oxidation and thereafter greatly enhanced $^1\text{O}_2$ selectivity to almost 100% [23]. However, it is worth noting that $^1\text{O}_2$ selectivity in this paper was determined according to scavenging experiments, the contribution to the degradation of *p*-chlorophenol was confusedly used to represent $^1\text{O}_2$ production selectivity. The degradation contribution of $^1\text{O}_2$ would vary with pollutants because the second-order reaction rate constants between the pollutant and the active species also vary. $^1\text{O}_2$ selectivity for PMS activation should be an intrinsic property of catalysts that is entirely unrelated to pollutants. The selectivity of $^1\text{O}_2$ generation determined by the proportion of PMS consumption used to generate $^1\text{O}_2$ to the total PMS consumption could systematically reflect the ability of catalysts to selectively convert PMS into $^1\text{O}_2$. To date, there has been no attempt to achieve a highly selective conversion of PMS to $^1\text{O}_2$. The mechanism and controlling factors of $^1\text{O}_2$ selective generation should be further explored from the perspective of geometrical and electronic structures of the active center. Besides, the support is crucial in manipulating the electronic structure of the active metal sites and interactions with the reactants [24]. So far, the effect of the support on $^1\text{O}_2$ selective production is barely reported. SACs have a uniform active metal center with a well-defined configuration that serves as an ideal vehicle to study the detailed internal mechanism of $^1\text{O}_2$ generation process.

In order to gain an insight into the $^1\text{O}_2$ generation process and illustrate key determinants of $^1\text{O}_2$ selective generation, we firstly performed density functional theory (DFT) calculations to analyze the Gibbs free energy variation of the $^1\text{O}_2$ generation process and electronic structure characteristics of Co- N_4 moiety on graphite carbon nitride (g- C_3N_4) and nitrogen-doped graphene. Under the theoretical guidance, the corresponding catalysts were synthesized and the single Co atom anchored to an uneven g- C_3N_4 nanosheet (Co-SA/CMN) achieved high $^1\text{O}_2$ production selectivity and exhibited an excellent oxidation degradation efficiency. Construction of high spin state active metal sites and weakening π -electron delocalization on the support are proven strategies to precisely control $^1\text{O}_2$ generation in PMS activation.

2. Materials and methods

2.1. Chemicals

Peroxymonosulfate (PMS, $\text{KHSO}_5 \cdot 0.5\text{KHSO}_4 \cdot 0.5\text{K}_2\text{SO}_4$), 17 β -estradiol (E2), cyanuric acid, melamine, cobalt nitrate hydrate ($\text{Co}(\text{NO}_3)_3 \cdot 9\text{H}_2\text{O}$), 4-chlorobenzoic acid (pCBA), 4-nitrobenzoic acid (pNBA) and furfuryl alcohol (FFA), potassium thiocyanate (KSCN), atenolol (ATE), atrazine (ATZ), benzotriazole (BTZ), bezafibrate (BZF), carbamazepine (CBZ), metoprolol (MTP), diethyltoluamide (DEET) and acetamidophenol (APAP) were obtained from Alfa Aesar. 5-tert-Butoxycarbonyl-5-methyl-1-pyrroline-N-oxide (BMPO, 99.0%) and 2,2,6,6-tetramethylpiperidinyloxyl (TEMP) was obtained from DOJINDO. Analytical grade or better for all the chemicals.

For the toxicity assay, streptomycin, penicillin, Albumin Bovine V, Paraformaldehyde, Dulbecco's modified Eagle's medium/nutrient mixture F-12 (DMEM/F-12, 1:1) and Triton X-100 were obtained from Gibco (USA) and Solarbio (China). Cell Counting Kit-8 (CCK-8) for cytotoxicity test was obtained from Dojindo Molecular Technologies (Japan). The Total Intracellular ROS Assay Kit (KA4075) was obtained from Abnova (USA). Anti-rabbit IgG Fab2 Alexa Fluor 647 molecular probes and P-Histone H2A.X (S139) rabbit antibody were purchased from Cell Signaling Technology (USA). Hoechst 33342 was purchased from Biotium (USA). Antibody Alexa Fluor® plus 555 were obtained from Thermo Fisher Scientific (USA).

2.2. Preparation of Co-SA/CMN

First, a cobalt nitrate solution containing 20 g/L of cobalt was prepared. Second, 30 mL acetonitrile was mixed with 1 g of melamine (solution 1) and 1 g of cyanuric acid (solution 2) for 30 min, respectively. After that, 10 mL of cobalt nitrate solution was poured to solution 1 and stirred for another 30 min. Then, solution 1 and 2 were mixed together and stirred for another 30 min. The resulting mixture was filtered and washed to obtain the purple precursors. The precursors were dried in vacuum for 12 h and then heated to 550 °C in a tube furnace for 4 h under Ar atmosphere. After calcination, the samples were ground, washed and dried.

2.3. Characterization

The morphologies of the catalysts were observed by scanning electron microscopy (XL30 Sirion, FEI, accelerating voltage 5 kV) and transmission electron microscopy (Tecnai G2 F30, FEI, accelerating voltage 300 kV). High-angle annular dark-field scanning transmission electron microscopy images were recorded on an aberration-corrected Thermo Fischer Themis G2 60–300 transmission electron microscope operated at 300 kV. N_2 physisorption measurements were performed on an ASAP 2020 M+C equipment at 77 K. Specific surface area and pore size distribution were obtained by BET and BJH models, respectively. D8 Advance X-ray powder diffractometer (XRD) with CuK α radiation ($\lambda = 1.5418 \text{ \AA}$) was used to obtain the crystalline structure. X-ray photoelectron spectra were recorded on a PHI5000VersaProbeII (Thermo Fisher) equipment with monochromatic Al K α source. Binding energies were calibrated by revising the measured binding energy of C 1 s to 284.8 eV. Raman spectra were acquired by HORIBA LabRAM HR800 system with 785 nm visible green laser light source. The metal loading and leaching was measured by an Optima 7300 DV inductively coupled plasma mass spectrometer (ICP-MS). The electron paramagnetic resonance (EPR) spectra were collected by a BRUKER E500 EPR device at room temperature. X-ray absorption fine structure (XAFS) spectra of Co K edge was collected at beamline TLS07A1, National Synchrotron Radiation Research Center (NSRRC) of Taiwan, China (The storage rings of NSRRC were operated at 1.5 GeV with an average current of 250 mA). The data were recorded by a silicon (220) monochromator in fluorescence mode. Energy was calibrated by pure Cu foil.

2.4. Catalytic Activity Measurements

Co-SA/CMN or CMN (0.1 g/L) was mixed with E2 solution (1 mg/L) and stirred for 60 min to establish an adsorption-desorption equilibrium. The, PMS (0.1 mM) was added to start the reaction. 1 mL of the sample was taken at certain time interval and quenched with 50 μ L of $\text{Na}_2\text{S}_2\text{O}_3$ (0.1 M). The sample was then filtered with cellulose acetate membrane (0.22 μ m).

2.5. Quantification of organic contaminants and intermediated identification

The pollutant concentrations were measured by high performance liquid chromatography (HPLC, SPD-M20A, Shimadzu) with a C18 reversed-phase column (Athena C18, 250 mm \times 4.6 mm, CNW). E2 was measured with fluorescent detector at an excitation wavelength of 280 nm and an emission wavelength of 310 nm [25], other pollutants or probes were determined by photo-diode array. The degradation intermediates of E2 were identified by an ultra-high-resolution hybrid quadrupole Orbitrap mass spectrometer (Q Exactive, Thermo Fisher Scientific) coupled with ultra-performance liquid chromatography (Ultimate 3000, Thermo Fisher Scientific) and Hypersil Gold C18 column (2.1 \times 100 mm, Thermo Fisher Scientific). The parameters for mass spectra and UPLC test condition were set according to our previous research [26].

2.6. Computational Models and Methodology

Theoretical calculations were performed based on spin-polarized density functional theory (DFT) [27] with Vienna ab initio simulation package (VASP) [28,29]. The electron exchange and correlation energies were treated within the generalized gradient approximation in the Perdew–Burke–Ernzerhof formalism (GGA-PBE) [30,31]. The projector augmented wave (PAW) pseudopotential was used to describe electron-ion interaction [32]. Specifically, the valence/outer-core electrons that are included in the self-consistent-field calculations are listed in parentheses for each atom: Co (3d⁸ 4s¹), O (2s² 2p⁴), S (3s² 3p⁴), C (2s² 2p²), and H (1s¹). The cutoff energy was set to 450 eV, K-point was set to Gamma point with 4 \times 4 \times 1 sampling for all optimization calculations. The convergence criteria for energy and force were set to 10^{−4} eV and 0.03 eV \AA^{-1} , respectively. Singlet and triplet oxygen has been initially tested with the above setting, showing an energy difference of 0.91 eV, which is close to experimental data [33]. Van der Waals (vdW) interaction was considered at the DFT-D2 level as proposed by Grimme [34]. The charge density and electron transfer were analyzed by the Bader code [35]. The LOBSTER 3.1.0 package was used to calculate the crystal orbital Hamilton population (COHP) based on projection of the delocalized PAW into localized atomic-like basis sets. Integrated COHP (ICOHP) was calculated by integrating the energy up to the Fermi level [36–38]:

$$\text{ICOHP} = \int_{\epsilon_F}^{\epsilon_F} \text{COHP}(E) dE$$

3. Results and Discussion

3.1. Mechanism of ¹O₂ selective production

A model of single-atom Co-N₄ configuration on g-C₃N₄ was constructed and compared with single atom Co-N₄ on graphene, which was reported to have ¹O₂ production capacity [39]. The Gibbs free energy variation and reaction pathway of ¹O₂ generation on Co-N₄/g-C₃N₄ and Co-N₄/graphene are shown in Fig. 1a, Fig. 1b, Fig. S1 and Fig. S2. The first process is the stepwise adsorption of two PMS molecules (PMS co-adsorption). For Co-N₄/g-C₃N₄, PMS co-adsorption was spontaneous with an energy drop of 0.26 eV and 1.19 eV, respectively. The uneven

surface of g-C₃N₄ and the electronegativity difference between carbon and nitrogen (N, 3.0 vs C, 2.5) both disturbed the mobility of free charge carriers and formed centers of positive (C) and negative charges (N) that were beneficial to the co-adsorption (Table S1 and Table S2) [40]. Beyond that, a significant energy decrease of PMS dissociated adsorption was observed that could be ascribed to the chemical adsorption between the Co atom and PMS. Then, SO₄^{•−} on the Co atom preferentially desorbed because it could release greater steric hindrance and lead to a higher energy drop (Fig. S1 (S4a)). Next, O in OH[•] absorbs O in O–O of SO₅^{•−}, resulting in the breaking of the O–O bond, forming two O[•]. At the same time, the H atom was transferred to another SO₄^{•−}, forming SO₄H[•], which was adsorbed by Co (Fig. S1 (S5a)) and desorbed subsequently. Two O[•] prefer to transfer to ¹O₂ directly (Fig. S1 (S6b)), rather than self-recombine to generate O₂ first because during the O–O reaction, C–O–O–C as the intermediate did not have a π bond and energy level degeneracy would not occur. The unpaired electron in oxygen was more prone to pair with the unpaired electron in the other oxygen atom. The triplet oxygen, which had two unpaired electrons, was barely formed because of the lack of degenerate energy levels. This step is also the rate-determining step with an energy barrier of 1.04 eV.

Although ¹O₂ formation on Co-N₄/graphene followed a similar reaction pathway to Co-N₄/g-C₃N₄ including PMS co-adsorption, breaking the O–O bond in PMS and [•]O interaction, ¹O₂ is harder to form on Co-N₄/graphene for two reasons. First, PMS co-adsorption did not easily happen because of the electrostatic repulsion and steric hindrance between [•]SO₅ and [•]HSO₅. The delocalized π -conjugated electrons in graphene also electrostatically repelled PMS ions. Second, [•]HSO₅ dissociated adsorption was difficult to happen on Co-N₄/graphene because of the limited electron transfer capacity of Co-N₄ active sites on graphene as demonstrated by the charge density and Bader charge analysis (Fig. S3, Table S3). Less electron transfer happened between PMS and Co-N₄/graphene. Thus, OH[•] was difficult to release, whereas the formation of [•]OH is essential for subsequent O–O breakage and ¹O₂ formation, which is reflected in the high energy barrier (2.0 eV) of the co-adsorption dissociation step (Fig. 1b). Co-N₄/graphene is not an efficient system for generating ¹O₂.

The partial density of states (pDOS) of the two structures are shown in Fig. 1c, d. The Co 3d orbital electron distribution in Co-N₄/g-C₃N₄ did not localize. However, Co-N₄/graphene showed a local distribution of 3d electrons at deep energy levels (red arrow in Fig. 1d), indicating that the Co atom lost its outer electrons, and was significantly oxidized. However, Co atoms in Co-N₄/g-C₃N₄ still retained their metallicity, as shown by the Bader charge analysis, Co atoms in Co-N₄/g-C₃N₄ kept more electrons (Table S3) because Co is a ferromagnetic element with three unpaired electrons. The deep oxidation that was represented by electron local distribution meant the loss of unpaired electrons, and finally led to a low spin state. The magnetic moments of Co-N₄/g-C₃N₄ and Co-N₄/graphene were 2.74 μ_B and 0.98 μ_B , respectively, indicating that Co on nitrogen-doped graphene was in a low spin state, but Co on g-C₃N₄ still preserved the high spin state and metallicity. The metallicity preservation was beneficial to forming chemical bonding while interacting with an oxidizing group such as PMS, as demonstrated by the crystal orbital Hamilton population (COHP) analysis of Co–O bonds in Fig. S4. The positive and negative parts of COHP over occupied states (below the Fermi level) correspond to the bonding and antibonding states that could stabilize and destabilize the Co–O bonding, respectively. For quantitative analysis, the integrated COHP (ICOHP) values were calculated. A more negative ICOHP value indicates a stronger bond strength [41,42]. Co-N₄/g-C₃N₄ possesses more negative ICOHP for PMS adsorption, indicating stronger Co–O bonding strength. Moreover, metallicity preservation could avoid spontaneous dissociation of adsorbed individual PMS molecules, which results in the formation of [•]OH and SO₄^{•−} [22]. Above all, PMS co-adsorption and dissociation were the key steps for ¹O₂ generation, and Co-N₄/g-C₃N₄ has two unique advantages in ¹O₂ selective production: (1) electron localization on support with distinct distribution of positive and negative charge centers

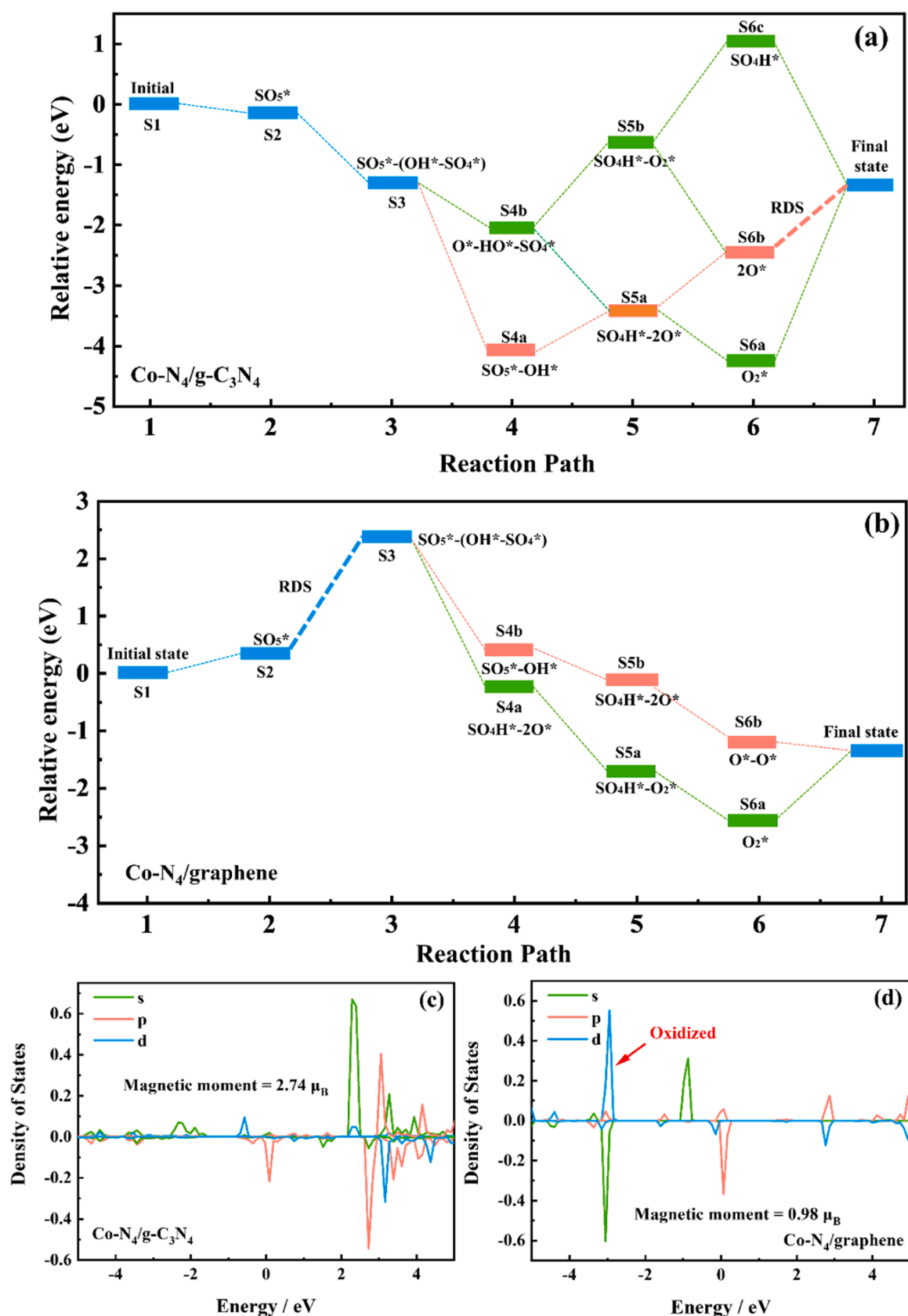


Fig. 1. DFT studies of $^1\text{O}_2$ generation on Co-N₄/g-C₃N₄ and Co-N₄/graphene. (a, b) Gibbs free energy diagram of $^1\text{O}_2$ generation pathway on Co-N₄/g-C₃N₄ and Co-N₄/graphene. (c, d) Partial density of states (pDOS) of Co atom on Co-N₄/g-C₃N₄ and Co-N₄/graphene.

was beneficial to overcome steric hindrance and electrostatic repulsion of PMS; (2) high spin state promoted spin oriented electron transfer, which favored the chemical adsorption and dissociation of persulfate adsorbates on the metal sites.

3.2. Synthesis and characterization of Co-SA/CMN

Based on the theoretical design, a single-atom catalyst with Co atomically dispersed on uneven graphite carbon nitride was synthesized using a molecular self-assembly strategy [43]. The porous and uneven morphology was evidenced by scanning electron microscopy (SEM) and transmission electron microscopy (TEM) images (Fig. S5a–c and Fig. S6a–c). Anchoring single Co atom to CMN showed little influence on the external morphology of CMN (Fig. 2a, Fig. S5d–f and Fig. S6d–f), but it increased the surface porosity of CMN. Fig. S7 shows that the Brunauer–Emmett–Teller (BET) surface area increased from 19.50 to 26.17 m²/g and the Barrett–Joyner–Halenda (BJH) pore volume increased from 0.15 to 0.41 cm³/g, after Co atom insertion. Fig. S8 shows two characteristic X-ray diffraction (XRD) peaks at 27.2° and 12.9°, which assigned to (002) interlayer stacking and (100) crystal plane from the trigonal nitrogen linkage of tri-s-triazine units, respectively [44,45]. With decreasing intensity for Co-SA/CMN compared with bare CMN, the insertion of Co atom distorts the crystal structure of CMN. No other peaks except for those from the g-C₃N₄ were detected. A high-resolution (HR) TEM image indicated no nanoparticles or clusters on Co-SA/CMN (Fig. 2b–d). The Co distribution at atomic resolution was also confirmed by aberration-corrected HAADF-STEM (AC HAADF-STEM) measurement. Plenty of bright spots were attributed to atomically dispersed cobalt atoms on g-C₃N₄ (Fig. 2e). The homogeneous distribution of Co was evidenced by energy-dispersive X-ray spectroscopy (EDX) mappings (Fig. 2f).

X-ray absorption fine structure (XAFS) and X-ray photoelectron spectra (XPS) were conducted to probe the coordination environment and electronic structure of Co sites in the Co-SA/CMN. According to the XPS survey, the synthesized Co-SA/CMN contained C, N and trace O (Fig. S9). The content of Co in Co-SA/CMN is 0.7%, which is not abundant enough to be distinguished by XPS. Coordination-unsaturated

in-plane N atoms in g-C₃N₄ are easily formed during thermal polymerization, which is crucial to achieve atomically dispersion [40,46]. Fig. 3a shows the N 1s XPS spectra of CMN and Co-SA/CMN. The characteristic peaks correspond to the sp² C=N – C bonds in the tri-s-triazine (pyridinic N) (398.7 eV), tertiary and secondary nitrogen (N-(C)₃ and C–NH–C groups (400.2 eV), N–H groups (401.3 eV) and π – π^* excitations between the stacking interlayers (404.1 eV), respectively [45,47]. The dominant nitrogen species was pyrrolic-N, which was more favorable for binding single Co atoms [48,49]. The N 1s XPS signal of Co-SA/CMN attributed to pyridinic N moved to the lower binding energy region compared to CMN suggesting that pyridinic N may coordinate with Co atoms to form the Co–N_x moieties. C did not coordinate with Co as shown by the similar C 1s spectra of Co-SA/CMN and CMN (Fig. S10). As shown in the X-ray absorption near-edge structure (XANES) spectra (Fig. 3b), the absorption edge position and white line peak of Co-SA/CMN are between Co foil and CoO, revealing that the valence state of Co in Co-SA/CMN is between 0 and +2. The Fourier-transformed (FT) k³-weighted extended X-ray absorption fine structure (EXAFS) spectra of Co-SA/CMN exhibited a prominent peak at 1.43 Å which is ascribed to the Co–N first shell, no characteristic Co–Co peak at about 2.1 Å was detected (Fig. 3c) [50]. Co–N coordination and atomical dispersion of Co were further confirmed according to the intensity maximum at 5 Å^{−1} in the EXAFS wavelet transform plots of Co-SA/CMN and cobalt phthalocyanine (CoPc) (Fig. S11). Furthermore, as shown in Fig. 3d, the Fourier transforms of the Co K edge EXAFS spectra of Co-SA/CMN were fitted well with the scattering path of Co–N. The best-fitting results show that the coordination number is 4.2 and the average Co–N bond length is about 2.03 Å (Table S4). All these results demonstrated the single atom Co–N₄ coordination configuration in Co-SA/CMN.

3.3. ¹O₂ production selectivity and degradation activity of the Co-SA/CMN/PMS system

The reactive species generated in the Co-SA/CMN/PMS system were detected using electron spin resonance. As a comparison, a catalyst with single cobalt atoms anchored on nitrogen-doped graphene (Co-SA/

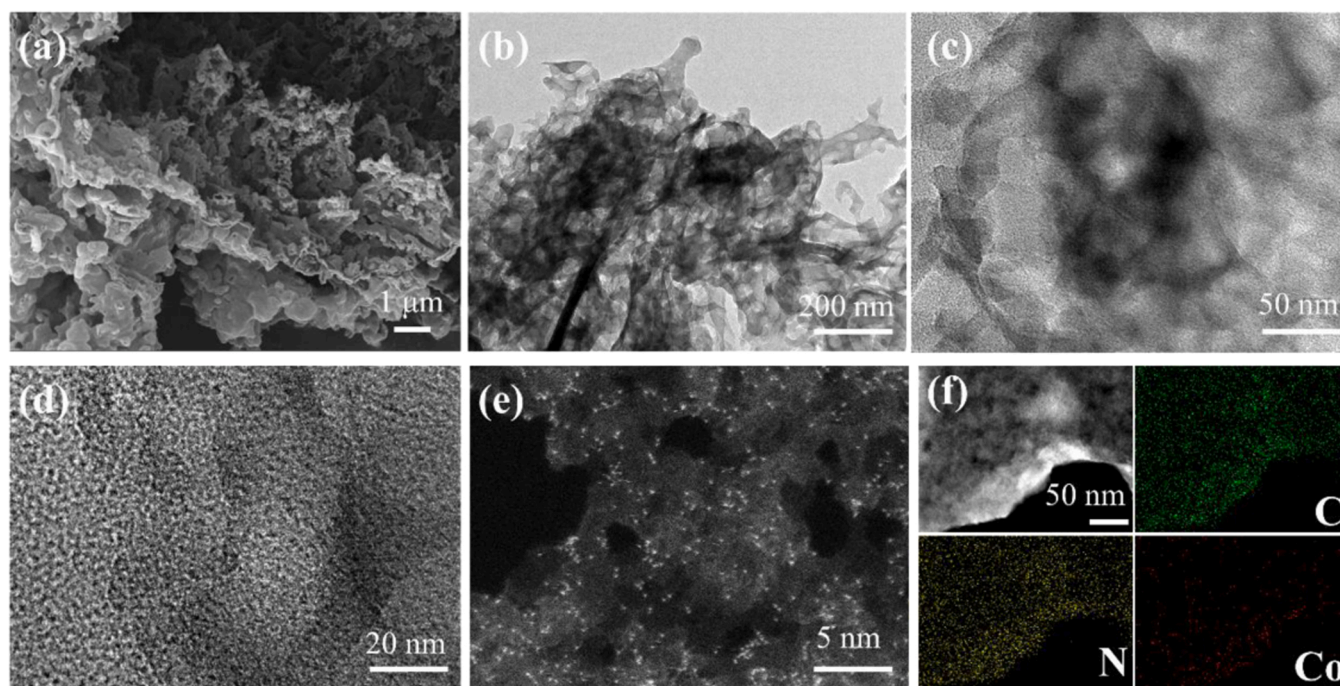


Fig. 2. Structural characterizations of Co-SA/CMN. (a) SEM. (b, c, d) HRTEM. (e) AC HAADF-STEM images of Co-SA/CMN. (f) Energy-dispersive X-ray elemental mapping of Co-SA/CMN.

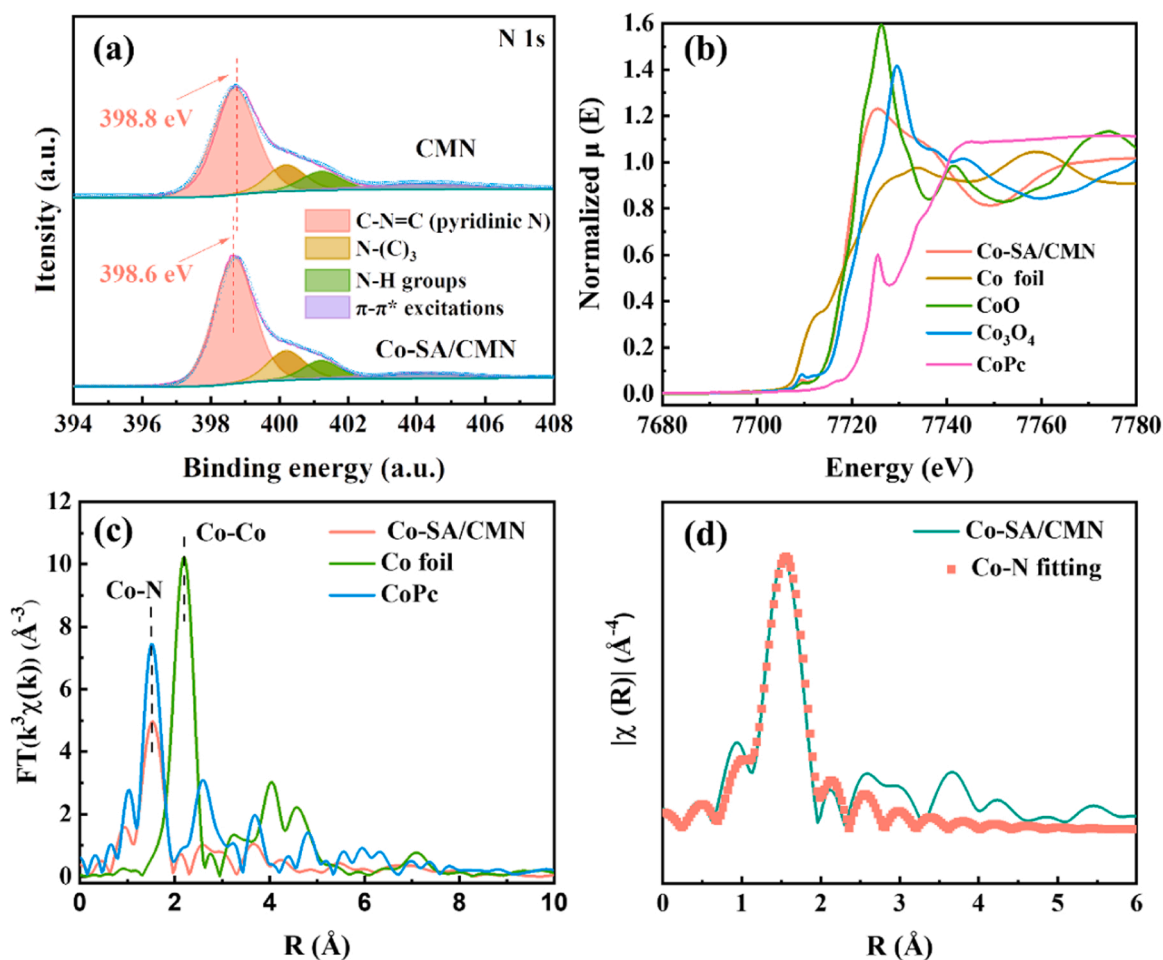


Fig. 3. Atomic structural analysis of Co-SA/CMN. (a) N 1 s XPS spectra of Co-SA/CMN and bare CMN. (b) Normalized Co K-edge XANES spectra of Co foil, CoO, Co₃O₄, CoPc, and Co-SA/CMN. (c, d) k³-weighted Fourier transform spectra from Co K edge EXAFS and the corresponding EXAFS fitting curve of Co-SA/CMN.

graphene) was synthesized according to a method reported previously [22]. The triplet signals of TEMP-¹O₂ were both observed in these two systems, but the intensity in the Co-SA/CMN/PMS system was much more significant than that in the Co-SA/graphene/PMS system (Fig. 4a). •OH and SO₄^{•−} were also both found in two systems (Fig. S12). Furthermore, we quantitatively measured the ¹O₂ production and PMS consumption to evaluate the selective conversion efficiency of PMS to ¹O₂ based on the stoichiometric ratio of ¹O₂ and PMS (1:2) [51]. Co-SA/CMN/PMS consumed PMS steadily and exhibited a high ¹O₂ production selectivity. On average, 87.8% of PMS was converted to ¹O₂ (Fig. 4b, Fig. S13). Co-SA/graphene consumed PMS quickly, but only 3.6% of PMS was converted to ¹O₂. The ¹O₂-oriented PMS conversion indicated the potential strong oxidation capacity of the Co-SA/CMN/PMS system in organic pollutant removal.

Estrogenic chemicals, which mimic steroid hormone activity, have been reported to be harmful to human health. In particular, E2 is by far the most estrogenic chemical [52]. E2 is several thousands of times more potent as an endocrine disruptor than other synthetic chemicals such as bisphenol A. Even at environmentally relevant concentrations of 0.1–20 ng/L, E2 can result in significant endocrine-disrupting effects [53,54]. Conventional chemical and biological processes could not remove estrogenic chemicals adequately, resulting in the concentration of E2 in groundwater or river water ranging from 6 to 66 ng/L [55]. ¹O₂-dominated oxidation systems are typically not effective for E2 degradation because of the relatively low second-order rate constant between ¹O₂ and E2 (7 × 10⁸ M^{−1} s^{−1}) [56,57]. However, the Co-SA/CMN/PMS system degraded E2 efficiently with the observed

reaction rate constant (*k*_{obs}) as high as 0.41 min^{−1} which is 3.1 times higher than that in Co-SA/graphene/PMS system (Fig. 4c). The leached solution has negligible catalytic degradation activity.

The active sites and dominant reactive species responsible for E2 removal in Co-SA/CMN system were explored. Thiocyanate (SCN[−]) is well-known to have a high affinity to cobalt which can poison the isolated cobalt sites through complexation in cobalt-catalyzed reactions. SCN[−] was hardly degraded during Co-SA/CMN/PMS oxidation (Fig. S14). However, as shown in Fig. S15, the addition of 0.2 mM SCN[−] evidently suppressed E2 degradation and 2 mM SCN[−] almost completely inhibited, reflecting that the single Co atoms are active sites for PMS conversion. In situ Raman spectra were performed to further analyze surface chemical evolution of Co-N₄ sites during PMS activation. The new peak at 830 cm^{−1} was assigned to the bonding between peroxo species and metal active sites (metal-PMS*) (Fig. S16) [58]. All these results implied that single-atom Co-N moieties were the catalytic active center for PMS activation [59].

The contributions of ¹O₂, •OH and SO₄^{•−} to E2 degradation in Co-SA/CMN were distinguished by a scavenging experiment and quantified by a competing kinetics calculation. The concentrations of quenchers which could directly react with PMS have been optimized to minimize their influence of direct PMS consumption on E2 degradation. As shown in Fig. 4d and Fig. S17, EtOH (scavenger for •OH and SO₄^{•−}) and tertiary butanol (TBA, scavenger for •OH) only exhibited slight inhibition on the E2 degradation even with dosage of 500 mM, which means that both •OH and SO₄^{•−} are not the dominant oxidants. In contrast when furfuryl alcohol (FFA) and NaN₃, specific scavengers for ¹O₂ were added, the

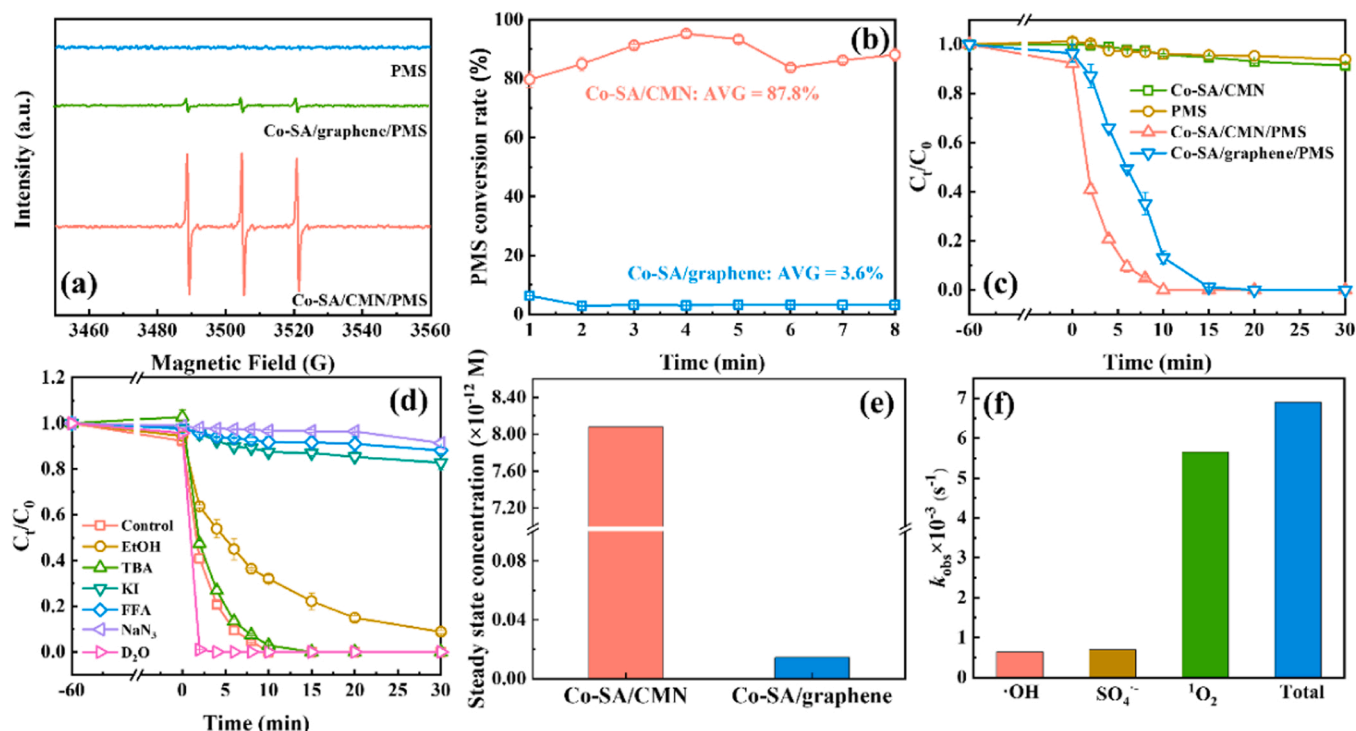


Fig. 4. $^1\text{O}_2$ production selectivity and oxidation capacity of Co-SA/CMN/PMS system. (a) EPR spectra of the different systems captured by TEMP (60 mM). (b) PMS to $^1\text{O}_2$ conversion rate in the Co-SA/CMN system. (c) E2 degradation performance in different reaction systems. (d) Quenching and solvent exchange experiments of the Co-SA/CMN/PMS system using EtOH (0.5 M), TBA (0.5 M), FFA (0.01 M), NaN_3 (0.02 M), and KI (0.04 M) as scavengers. (e) Steady-state concentrations of $^1\text{O}_2$ in Co-SA/CMN/PMS and Co-SA/graphene/PMS systems. (f) Contributions of different active species to E2 degradation in the Co-SA/CMN/PMS system. Reaction condition: [Catalyst] = 0.1 g/L, [PMS] = 0.1 mM, [E2] = 1 mg/L, initial pH = 7, T = 298 K.

efficiency of E2 degradation was significantly inhibited with k_{obs} reduced from 0.414 min^{-1} to 0.009 min^{-1} and 0.003 min^{-1} , respectively (Fig. S17), suggesting the crucial role of $^1\text{O}_2$. Moreover, KI, a strong scavenger for surface-bound free radicals [60], also significantly quenched the reaction with k_{obs} decreasing to 0.019 min^{-1} , demonstrating that E2 was likely decomposed by reacting with surface-generated $^1\text{O}_2$. A solvent exchange experiment (H_2O to deuterium oxide (D_2O)) was performed to verify the key role of $^1\text{O}_2$, because $^1\text{O}_2$ has a much longer lifetime in D_2O than in H_2O [61,62]. The degradation kinetics of E2 was significantly accelerated in D_2O , further confirming the main role of $^1\text{O}_2$ in E2 degradation (Fig. 4d and Fig. S17). Furthermore, we quantified the steady-state concentrations of ROS in Co-SA/CMN/PMS and Co-SA/graphene/PMS systems with correspond ROS probes and competing kinetic calculation (Fig. S18 and Fig. S19). Specific experiment and calculation steps are listed in Text S1. In Co-SA/CMN/PMS system, the steady-state concentration of $^1\text{O}_2$ was 25 times higher than $\text{SO}_4^{\cdot-}$ and 200 times higher than $\cdot\text{OH}$, which is consistent with the high $^1\text{O}_2$ production selectivity (Fig. S20). Co-SA/CMN/PMS system also has the $^1\text{O}_2$ steady-state concentration and corresponding E2 degradation efficiency of $^1\text{O}_2$ 560 times higher than those of Co-SA/graphene/PMS system (Fig. 4e), which was consistent with the results of PMS conversion selectivity and theoretical calculation conclusions. As shown in Fig. 4f and S21, $^1\text{O}_2$ was responsible for 80.6% of the total E2 degradation, but $^1\text{O}_2$ only contributed 0.5% to E2 degradation in the Co-SA/graphene/PMS system, indicating that increasing $^1\text{O}_2$ production selectivity is beneficial to expanding the contribution of $^1\text{O}_2$ to pollutant degradation and improving the degradation efficiency. By virtue of the high steady-state concentration of $^1\text{O}_2$ and multiple reactive species generation, Co-SA/CMN/PMS system also shows powerful oxidation capacity to various organic contaminants including atenolol (ATE), bezafibrate (BZF), carbamazepine (CBZ), metoprolol (MTP), *N,N*-diethyl-3-methyl benzoyl amide (DEET), acetamidophenol (APAP) and atrazine (ATZ) (Fig. S22).

Based on the oxidation selectivity for $^1\text{O}_2$, the Co-SA/CMN/PMS system exhibits strong resistance to environmental interference such as inorganic anions and organic matters [51,63–65]. Fig. S23a, b indicate that the Co-SA/CMN/PMS system had a good resistance to high concentration of ubiquitous inorganic ions in real water (Cl^- , CO_3^{2-} , SO_4^{2-} , NO_3^- , Ca^{2+} and Mg^{2+}). Most inorganic ions had no negative effect on the degradation of E2, only high concentration of NO_3^- and Mg^{2+} slightly retarded the E2 degradation. Humic acid and protein as representatives of organic matters in sewage partially suppressed the E2 degradation in Co-SA/CMN/PMS system (Fig. S23c). However, the inhibition effect is mainly due to the occupation of the active site by HA and BSA which are both negatively charged organic matters. The oxidation selectivity of the Co-SA/CMN/PMS system was still validated in more complicated real water samples (Table S5). Both the secondary effluent and tap water showed negligible influence and the livestock sewage diluent with much higher organic matters concentration only slightly retarded the on the degradation efficiency of Co-SA/CMN/PMS system (Fig. S23d). In comparison, Co^{2+} /PMS system, the recognized radical-based oxidation system, was almost completely inhibited for E2 degradation in secondary effluent and livestock sewage diluent (Fig. S23e), indicating the better anti-interference ability of Co-SA/CMN/PMS system. Fig. S24 shows that Co-SA/CMN as a PMS activator could maintain high degradation efficiency in a broad pH range. A neutral or weakly alkaline environment was preferred for Co-SA/CMN/PMS system.

Above all, Co-SA/CMN could activate the selective conversion of PMS to $^1\text{O}_2$, which endows the Co-SA/CMN/PMS system with superior oxidation capacity to a broad spectrum of recalcitrant pollutants and strong tolerance to environmental interference.

3.4. Long-term operating test and toxicity removal

Recyclability of the heterogeneous catalyst is crucial in practical

applications. The cycle experiment was conducted to evaluate the stability of Co-SA/CMN. After five cycles, the Co-SA/CMN/PMS system retained its original catalytic activity (Fig. 5a). No appreciable changes in chemical composition were observed (Fig. S25). The high catalytic activity and stability of Co-SA/CMN encouraged us to explore its performance further in a continuous-flow reactor. Fig. S26 and Fig. S27 show images of a Co-SA/CMN-based carbon felt filter (CSCF) and corresponding flow-through reactor. Carbon felt is highly porous with large surface area, which is conducive to achieving high catalyst loading and local pollutants enrichment. The strong and porous structure of carbon felt helps to resist the long period of water erosion without affecting water penetration and increases water turbulence to facilitate contact between the pollutant and reactive species. Moreover, the chemical inertness and low cost also increase its practical applicability. Bed volume (BV), which was defined as the ratio of treated water to the volume

of the filter, was used to assess the stability of filter in a flow-through reactor. E2 and PMS mixed solution was passed through the CSCF with retention time of only 15 s. The CSCF maintained almost 100% E2 removal for 36 h after 8800 BV (21.6 L of wastewater was filtered) and over 90% E2 removal for 48 h after 11734 BV (28.8 L of wastewater was filtered) (Fig. 5b). Meanwhile, the strong metal-support interaction helped to keep low leached Co in the whole process. Neither carbon felt with PMS nor CSCF alone was effective for E2 degradation (Fig. S28).

Although E2 was degraded after the Co-SA/CMN/PMS system treatment, many oxidation products may still preserve the structure with endocrine-disrupting effects and show environmental hazards. Therefore, several reaction products of E2 oxidized by the Co-SA/CMN/PMS system were detected using LC-MS negative ion mode (Table S6). The masses of pseudomolecular ions $[M - H]^-$ and relative chromatographic retention time were used to infer product structure [66]. Most of the

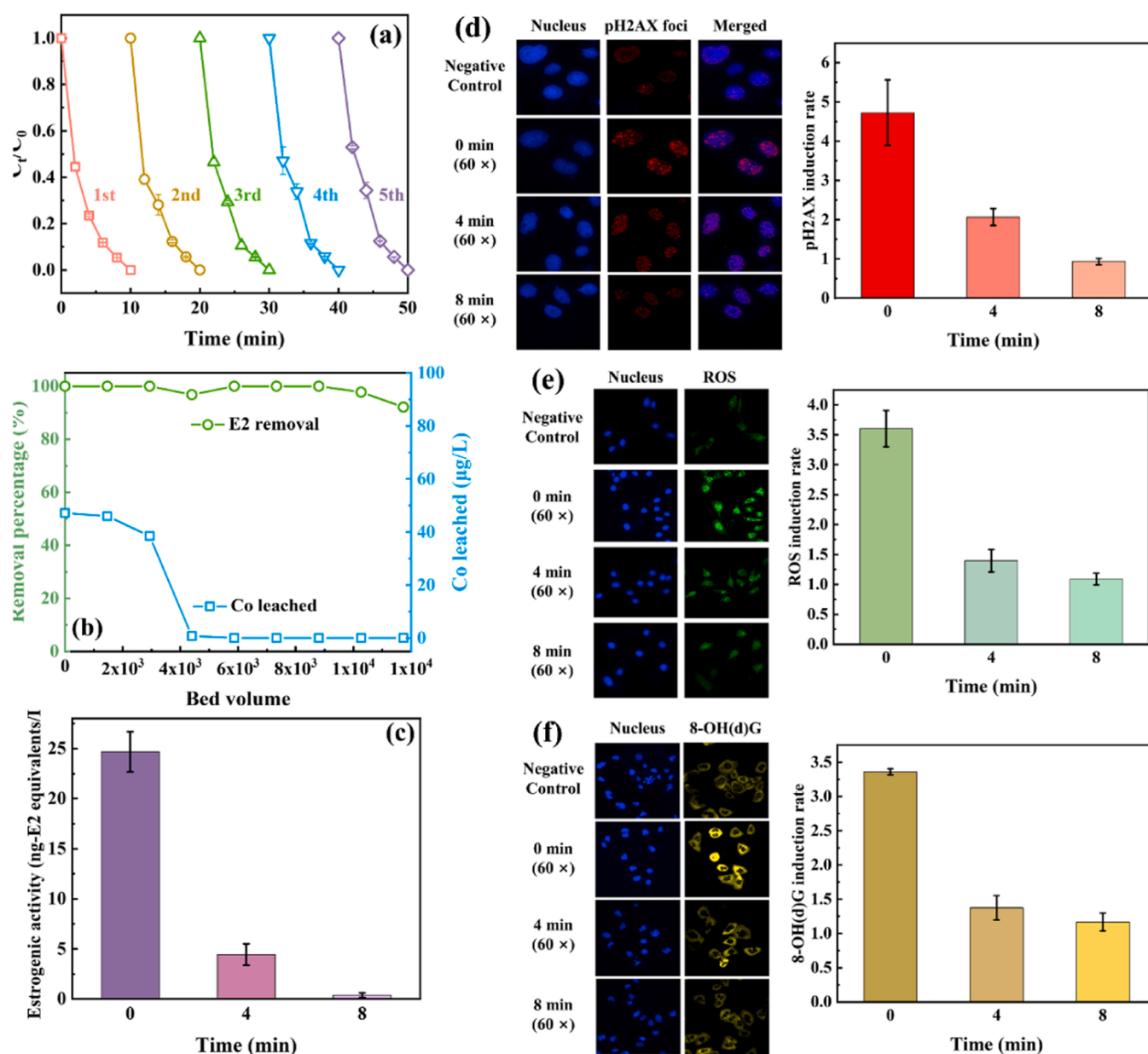


Fig. 5. Long-term operating test and toxicity removal. (a) The removal efficiency of Co-SA/CMN/PMS system in repeated batch catalytic reactions. (b) Continuous operation test of E2 degradation and Co leaching by the CSCF-based flow-through filter. Reaction condition: flow rate = 10 mL/min, Catalyst loading = 0.1 g, [PMS] = 0.1 mM, [E2] = 2 mg/L, initial pH = 7, T = 298 K. Bed volume (BV) means the volume of flow-through reactor which was employed to assess the performance of filter. (c) Estrogenic activity of E2 during Co-SA/CMN/PMS oxidation process. (d, e, f) Immunofluorescent staining images of CHO cells and induction rate of E2 samples with different degrees of oxidation by Co-SA/CMN/PMS system d) pH2AX, e) ROS, f) 8-OH(d)G.

supposed products have greater molecular weights which should be attributed to the formation of carboxyl, carbonyl or alcohol groups after oxygen insertion [67]. The commonness of product structure reveals that $^1\text{O}_2$ prefers to attack the hydroxyl group in the aromatic ring, resulting in a series of quinone-like and aromatic ring-opening products formation, but the alcohol and ethynyl groups in E2 keep intact. It has been reported that the strong estrogenic activity of steroid estrogens is mainly ascribed to the phenolic moiety. The quinone-like and aromatic ring-opening oxidation products with broken phenolic moieties should exhibit much weaker estrogenic potency [52,68,69]. The variation of estrogenic activity for E2 before and after oxidation with the Co-SA/CMN/PMS system were quantified by yeast two-hybrid assay. Fig. S29 illustrates the estrogenic activity–diluted E2 concentration relationship curve. Fig. 5c shows that the estrogenic activity of the samples before oxidation was 24.7 ng-E2 equivalents/L. After 4 and 8 min oxidation, the estrogenic activities decreased to 4.4 and 0.2 ng-E2 equivalents/L, respectively. Except for estrogenic activities, E2 could also induce double-strand breaks (DSBs) and genomic instability, which cause the initiation and progression of breast cancer [70]. Measuring pH2AX could quantitatively reflect the degree of DNA DSBs because of the one-to-one relationship between phosphorylated histone H2AX (pH2AX) and DNA DSBs [71]. E2 could induce pH2AX foci accumulation in CHO cells, but pH2AX foci numbers were significantly decreased after E2 was oxidized by Co-SA/CMN/PMS. The pH2AX induction rate decreased from 5.6 to 2.0 after 4 min and even comparable to the control group after 8 min (Fig. 5d). Moreover, the oxidative stress from metabolic activation of E2 may cause DNA oxidative damage and lead to estrogen-induced carcinogenesis [72,73]. The ROS induced by E2 before and after Co-SA/CMN/PMS treatment were evaluated. Images in the ROS measurement showed that E2 exposure could induce significant ROS formation, but the induced ROS was less in samples treated with Co-SA/CMN/PMS (Fig. 5e). The ROS induction rates were decreased from 3.6 to 1.4 and 1.1 after treating E2 with Co-SA/CMN/PMS for 4 and 8 min, respectively (Fig. 5e). A decrease in ROS production should also lead to a remission in DNA oxidative damage. 8-Hydroxy-deoxyguanosine and 8-hydroxy-guanosine (together labeled 8-OH(d)G) are produced through base modification at the C-8 position of guanine in deoxyguanosine and guanosine. The amount of 8-OH(d)G generation corresponds to the degree of DNA oxidative damage [74]. The immunofluorescent staining results indicated that E2 alone could induce lots of 8-OH(d)G (Fig. 5f). However, Co-SA/CMN/PMS oxidation significantly reduced the 8-OH(d)G induction rate by 1.4 and 1.2 for E2 samples oxidized for 4 and 8 min, respectively (Fig. 5f). Besides that, E2 as a typical endocrine disrupter will affect the normal metabolism of cells and exhibit cytotoxicity [75]. The cytotoxicity changes during Co-SA/CMN/PMS oxidation process were evaluated (Fig. S30). The samples before oxidation almost completely killed cells with cell viability only 3%. However, brief Co-SA/CMN/PMS system significantly increased cell survival to 51% and 98% after 4 and 8 min treatment, respectively.

Overall, Co-SA/CMN showed high stability and removal efficiency, which endowed the Co-SA/CMN-based carbon felt filter with satisfactory long-term operating performance and negligible leaching of metal ions. Moreover, the perniciousness of E2 as an endocrine disrupter was greatly reduced and no obviously toxic by-products were formed after Co-SA/CMN system oxidation. Co-SA/CMN/PMS system provides a safe solving strategy for the control of E2 risk in drinking water and wastewater.

4. Conclusions

DFT calculations demonstrated that PMS co-adsorption and dissociation were the key steps for $^1\text{O}_2$ generation, but electrostatic repulsion between PMS and π -electron delocalization in the support causes a high energy barrier for PMS co-adsorption and dissociation. Electron localization and construction of a high spin state active metal center are two

effective ways to reduce the energy barrier and enhance $^1\text{O}_2$ production selectivity. According to the guidance of the theoretical calculations, a single cobalt atom catalyst with Co- N_4 moieties embedded into tri-s-triazine units of an uneven graphite carbon nitride nanosheet was fabricated and showed $^1\text{O}_2$ production selectivity as high as 87.8%. In addition, the Co-SA/CMN/PMS system with a high steady-state concentration of $^1\text{O}_2$ could efficiently degrade E2 and remove the estrogenic activity and toxicity originating from E2. The Co-SA/CMN/PMS system also exhibits strong resistance to environmental disturbance and robust stability at the device level. These findings not only construct a heterogeneous catalytic oxidation system with high decontamination capacity, low cost, excellent resistance to interference from environmental impurities, long-term stability and safety which offer promising application in practical water purification, but also deepen the mechanistic understanding to the origins of high $^1\text{O}_2$ production selectivity and provide a rational strategy for precisely controlling $^1\text{O}_2$ generation in PMS activation.

CRediT authorship contribution statement

Zhi-Wei Wang: Methodology, Data curation; Formal analysis; Writing – original draft. **Yu Wang:** Formal analysis, Investigation. **Wen-Long Wang:** Writing – review & editing. **De-Xiu Wu:** Toxicity experiment. **Qian-Yuan Wu:** Conceptualization, Funding acquisition, Writing – review & editing. **Hong-Ying Hu:** Conceptualization, Funding acquisition, Writing – review & editing.

Declaration of Competing Interest

The authors declare that they have no known competing financial interests or personal relationships that could have appeared to influence the work reported in this paper.

Data Availability

Data will be made available on request.

Acknowledgments

This study was supported by National Natural Science Foundation of China (No. 52022049), and the Shenzhen Science, Technology and Innovation Commission (No. JCYJ20200109142829123). Thanks to TianHe-2, LvLiang Cloud Computing Center of China for providing computational resource.

Appendix A. Supporting information

Supplementary data associated with this article can be found in the online version at doi:10.1016/j.apcatb.2022.122248.

References

- [1] J.L. Cleveland, M.B. Kastan, A radical approach to treatment, *Nature* 407 (2000) 309–311.
- [2] U. Theopold, A bad boy comes good, *Nature* 461 (2009) 486–487.
- [3] H. Kautsky, Quenching of luminescence by oxygen, *Trans. Faraday Soc.* 35 (1939) 216–219.
- [4] Y. Lion, M. Delmelle, A. Van de Vorst, New method of detecting singlet oxygen production, *Nature* 263 (1976) 442–443.
- [5] Y. Zhao, M. Sun, X. Wang, C. Wang, D. Lu, W. Ma, S.A. Kube, J. Ma, M. Elimelech, Janus electrocatalytic flow-through membrane enables highly selective singlet oxygen production, *Nat. Commun.* 11 (2020) 1–10.
- [6] J. Al-Nu'airat, B.Z. Dlugogorski, X. Gao, N. Zeinali, J. Skut, P.R. Westmoreland, I. Oluwoye, M. Altarawneh, Reaction of phenol with singlet oxygen, *Phys. Chem. Chem. Phys.* 21 (2019) 171–183.
- [7] A.U. Khan, Singlet molecular oxygen from superoxide anion and sensitized fluorescence of organic molecules, *Science* 168 (1970) 476–477.
- [8] E. Skovsen, J.W. Snyder, J.D. Lambert, P.R. Ogilby, Lifetime and diffusion of singlet oxygen in a cell, *J. Phys. Chem. B* 109 (2005) 8570–8573.

- [9] Z. Zhou, J. Song, R. Tian, Z. Yang, G. Yu, L. Lin, G. Zhang, W. Fan, F. Zhang, G. Niu, Activatable singlet oxygen generation from lipid hydroperoxide nanoparticles for cancer therapy, *Angew. Chem. Int. Ed.* 129 (2017) 6592–6596.
- [10] P. Di Mascio, G.R. Martinez, S. Miyamoto, G.E. Ronsein, M.H. Medeiros, J. Cadet, Singlet molecular oxygen reactions with nucleic acids, lipids, and proteins, *Chem. Rev.* 119 (2019) 2043–2086.
- [11] Q. Yi, J. Ji, B. Shen, C. Dong, J. Liu, J. Zhang, M. Xing, Singlet oxygen triggered by superoxide radicals in a molybdenum cocatalytic Fenton reaction with enhanced REDOX activity in the environment, *Environ. Sci. Technol.* 53 (2019) 9725–9733.
- [12] V. Duarte, D. Gasparutto, L.F. Yamaguchi, J.-L. Ravanat, G.R. Martinez, M. H. Medeiros, P. Di Mascio, J. Cadet, Oxaluric acid as the major product of singlet oxygen-mediated oxidation of 8-oxo-7, 8-dihydroguanine in DNA, *J. Am. Chem. Soc.* 122 (2000) 12622–12628.
- [13] F. Manjón, L. Villén, D. García-Fresnadillo, G. Orellana, On the factors influencing the performance of solar reactors for water disinfection with photosensitized singlet oxygen, *Environ. Sci. Technol.* 42 (2008) 301–307.
- [14] J. Brame, M. Long, Q. Li, P. Alvarez, Trading oxidation power for efficiency: differential inhibition of photo-generated hydroxyl radicals versus singlet oxygen, *Water Res.* 60 (2014) 259–266.
- [15] A.D. Bokare, W. Choi, Singlet-oxygen generation in alkaline periodate solution, *Environ. Sci. Technol.* 49 (2015) 14392–14400.
- [16] Y. Jiang, J.E. Goodwill, J.E. Tobiasson, D.A. Reckhow, Bromide oxidation by ferrate (VI): The formation of active bromine and bromate, *Water Res.* 96 (2016) 188–197.
- [17] Q.-Y. Wu, Y.-T. Zhou, W. Li, X. Zhang, Y. Du, H.-Y. Hu, Underestimated risk from ozonation of wastewater containing bromide: Both organic byproducts and bromate contributed to the toxicity increase, *Water Res.* 162 (2019) 43–52.
- [18] D.E. Dolmans, D. Fukumura, R.K. Jain, Photodynamic therapy for cancer, *Nat. Rev. Cancer* 3 (2003) 380–387.
- [19] A.A. Ghogare, A. Greer, Using singlet oxygen to synthesize natural products and drugs, *Chem. Rev.* 116 (2016) 9994–10034.
- [20] X. Li, J. Wang, X. Duan, Y. Li, X. Fan, G. Zhang, F. Zhang, W. Peng, Fine-tuning radical/nonradical pathways on graphene by porous engineering and doping strategies, *ACS Catal.* 11 (2021) 4848–4861.
- [21] H. Li, C. Shan, B. Pan, Fe (III)-doped g-C₃N₄ mediated peroxymonosulfate activation for selective degradation of phenolic compounds via high-valent iron-oxo species, *Environ. Sci. Technol.* 52 (2018) 2197–2205.
- [22] X. Mi, P. Wang, S. Xu, L. Su, H. Zhong, H. Wang, Y. Li, S. Zhan, Almost 100% peroxymonosulfate conversion to singlet oxygen on single-atom CoN₂₊₂ sites, *Angew. Chem. Int. Ed.* 133 (2021) 4638–4643.
- [23] L.S. Zhang, X.H. Jiang, Z.A. Zhong, L. Tian, Q. Sun, Y.T. Cui, X. Lu, J.P. Zou, S. L. Luo, Carbon Nitride Supported High-Loading Fe Single-Atom Catalyst for Activation of Peroxymonosulfate to Generate ¹O₂ with 100% Selectivity, *Angew. Chem. Int. Ed.* 60 (2021) 21751–21755.
- [24] A. Wang, J. Li, T. Zhang, Heterogeneous single-atom catalysis, *Nat. Rev. Chem.* 2 (2018) 65–81.
- [25] Y. Yoon, P. Westerhoff, S.A. Snyder, M. Esparza, HPLC-fluorescence detection and adsorption of bisphenol A, 17 β -estradiol, and 17 α -ethynyl estradiol on powdered activated carbon, *Water Res.* 37 (2003) 3530–3537.
- [26] Y. Lu, Z.-M. Song, C. Wang, J.-K. Liang, N. Xu, Q. Hu, Q.-Y. Wu, Combination of high resolution mass spectrometry and a halogen extraction code to identify chlorinated disinfection byproducts formed from aromatic amino acids, *Water Res.* 190 (2021), 116710.
- [27] P. Hohenberg, W. Kohn, Density functional theory (DFT), *Phys. Rev.* 136 (1964) B864.
- [28] P.E. Blöchl, O. Jepsen, O.K. Andersen, Improved tetrahedron method for Brillouin-zone integrations, *Phys. Rev. B* 49 (1994) 16223.
- [29] G. Kresse, J. Furthmüller, Efficient iterative schemes for ab initio total-energy calculations using a plane-wave basis set, *Phys. Rev. B* 54 (1996) 11169.
- [30] M.C. Payne, M.P. Teter, D.C. Allan, T. Arias, a.J. Joannopoulos, Iterative minimization techniques for ab initio total-energy calculations: molecular dynamics and conjugate gradients, *Rev. Mod. Phys.* 64 (1992) 1045.
- [31] W. Kohn, L.J. Sham, Self-consistent equations including exchange and correlation effects, *Phys. Rev.* 140 (1965) A1133.
- [32] G. Kresse, D. Joubert, From ultrasoft pseudopotentials to the projector augmented-wave method, *Phys. Rev. B* 59 (1999) 1758.
- [33] D.R. Kearns, Physical and chemical properties of singlet molecular oxygen, *Chem. Rev.* 71 (1971) 395–427.
- [34] S. Grimme, Semiempirical GGA-type density functional constructed with a long-range dispersion correction, *J. Comput. Chem.* 27 (2006) 1787–1799.
- [35] W. Tang, E. Sanville, G. Henkelman, A grid-based Bader analysis algorithm without lattice bias, *J. Phys. Condens. Matter* 21 (2009), 084204.
- [36] R. Dronskowski, P.E. Blochl, Crystal orbital Hamilton populations (COHP): energy-resolved visualization of chemical bonding in solids based on density-functional calculations, *J. Phys. Chem.* 97 (1993) 8617–8624.
- [37] S. Maintz, V.L. Deringer, A.L. Tchougréeff, R. Dronskowski, LOBSTER: A tool to extract chemical bonding from plane-wave based DFT, *Wiley Online Libr.* (2016).
- [38] V.L. Deringer, A.L. Tchougréeff, R. Dronskowski, Crystal orbital Hamilton population (COHP) analysis as projected from plane-wave basis sets, *J. Phys. Chem. A* 115 (2011) 5461–5466.
- [39] X. Li, X. Huang, S. Xi, S. Miao, J. Ding, W. Cai, S. Liu, X. Yang, H. Yang, J. Gao, Single cobalt atoms anchored on porous N-doped graphene with dual reaction sites for efficient Fenton-like catalysis, *J. Am. Chem. Soc.* 140 (2018) 12469–12475.
- [40] W.-J. Ong, L.-L. Tan, Y.H. Ng, S.-T. Yong, S.-P. Chai, Graphitic carbon nitride (g-C₃N₄)-based photocatalysts for artificial photosynthesis and environmental remediation: are we a step closer to achieving sustainability? *Chem. Rev.* 116 (2016) 7159–7329.
- [41] J. Zhu, M. Xiao, D. Ren, R. Gao, X. Liu, Z. Zhang, D. Luo, W. Xing, D. Su, A. Yu, Quasi-covalently coupled Ni–Cu Atomic Pair for Synergistic Electroreduction of CO₂, *J. Am. Chem. Soc.* (2022).
- [42] Q. Wang, Z. Zhang, C. Cai, M. Wang, Z.L. Zhao, M. Li, X. Huang, S. Han, H. Zhou, Z. Feng, Single iridium atom doped Ni₂P catalyst for optimal oxygen evolution, *J. Am. Chem. Soc.* 143 (2021) 13605–13615.
- [43] Y. Zheng, J. Liu, J. Liang, M. Jaroniec, S.Z. Qiao, Graphitic carbon nitride materials: controllable synthesis and applications in fuel cells and photocatalysis, *Energy Environ. Sci.* 5 (2012) 6717–6731.
- [44] G. Zhang, J. Zhang, M. Zhang, X. Wang, Polycondensation of thiourea into carbon nitride semiconductors as visible light photocatalysts, *J. Mater. Chem.* 22 (2012) 8083–8091.
- [45] S. An, G. Zhang, T. Wang, W. Zhang, K. Li, C. Song, J.T. Miller, S. Miao, J. Wang, X. Guo, High-density ultra-small clusters and single-atom Fe sites embedded in graphitic carbon nitride (g-C₃N₄) for highly efficient catalytic advanced oxidation processes, *ACS Nano* 12 (2018) 9441–9450.
- [46] Q. Tay, P. Kanhere, C.F. Ng, S. Chen, S. Chakraborty, A.C.H. Huan, T.C. Sum, R. Ahuja, Z. Chen, Defect engineered g-C₃N₄ for efficient visible light photocatalytic hydrogen production, *Chem. Mater.* 27 (2015) 4930–4933.
- [47] Q. Zheng, D.P. Durkin, J.E. Elenewski, Y. Sun, N.A. Banek, L. Hua, H. Chen, M. J. Wagner, W. Zhang, D. Shuai, Visible-light-responsive graphitic carbon nitride: rational design and photocatalytic applications for water treatment, *Environ. Sci. Technol.* 50 (2016) 12938–12948.
- [48] J. Li, S. Ghoshal, W. Liang, M.-T. Sougrati, F. Jaouen, B. Halevi, S. McKinney, G. McCoil, C. Ma, X. Yuan, Structural and mechanistic basis for the high activity of Fe–N–C catalysts toward oxygen reduction, *Energy Environ. Sci.* 9 (2016) 2418–2432.
- [49] K. Artyushkova, A. Serov, S. Rojas-Carbonell, P. Atanassov, Chemistry of multitudinous active sites for oxygen reduction reaction in transition metal–nitrogen–carbon electrocatalysts, *J. Phys. Chem. C* 119 (2015) 25917–25928.
- [50] H. Fei, J. Dong, Y. Feng, C.S. Allen, C. Wan, B. Voloskiy, M. Li, Z. Zhao, Y. Wang, H. Sun, General synthesis and definitive structural identification of MN₄C₄ single-atom catalysts with tunable electrocatalytic activities, *Nat. Catal.* 1 (2018) 63–72.
- [51] L.S. Zhang, X.H. Jiang, Z.A. Zhong, L. Tian, Q. Sun, Y.T. Cui, X. Lu, J.P. Zou, S. L. Luo, Carbon nitride supported high-loading Fe single-atom catalyst for activation of peroxymonosulfate to generate ¹O₂ with 100% selectivity, *Angew. Chem. Int. Ed.* 60 (2021) 21751–21755.
- [52] Y. Zhao, J. Hu, W. Jin, Transformation of oxidation products and reduction of estrogenic activity of 17 β -estradiol by a heterogeneous photo-Fenton reaction, *Environ. Sci. Technol.* 42 (2008) 5277–5284.
- [53] C. Purdom, P. Hardiman, V. Bye, N. Eno, C. Tyler, J. Sumpter, Estrogenic effects of effluents from sewage treatment works, *Chem. Ecol.* 8 (1994) 275–285.
- [54] S. Jobling, M. Nolan, C.R. Tyler, G. Brighty, J.P. Sumpter, Widespread sexual disruption in wild fish, *Environ. Sci. Technol.* 32 (1998) 2498–2506.
- [55] E. Peterson, R. Davis, H. Orndorff, 17 β -estradiol as an indicator of animal waste contamination in Mantled Karst Aquifers, *Wiley Online Libr.* (2000).
- [56] R. Lyubimenko, O.I.G. Cardenas, A. Turshatov, B.S. Richards, A.I. Schäfer, Photodegradation of steroid-hormone micro pollutants in a flow-through membrane reactor coated with Pd (II)-porphyrin, *Appl. Catal. B Environ.* 291 (2021), 120097.
- [57] Y. Zhou, J. Jiang, Y. Gao, J. Ma, S.-Y. Pang, J. Li, X.-T. Lu, L.-P. Yuan, Activation of peroxymonosulfate by benzoquinone: a novel nonradical oxidation process, *Environ. Sci. Technol.* 49 (2015) 12941–12950.
- [58] K. Qian, H. Chen, W. Li, Z. Ao, Y.-n Wu, X. Guan, Single-atom Fe catalyst outperforms its homogeneous counterpart for activating peroxymonosulfate to achieve effective degradation of organic contaminants, *Environ. Sci. Technol.* 55 (2021) 7034–7043.
- [59] J. Miao, Y. Zhu, J. Lang, J. Zhang, S. Cheng, B. Zhou, L. Zhang, P.J. Alvarez, M. Long, Spin-state-dependent peroxymonosulfate activation of single-atom M–N moieties via a radical-free pathway, *ACS Catal.* 11 (2021) 9569–9577.
- [60] Z. Huang, H. Bao, Y. Yao, W. Lu, W. Chen, Novel green activation processes and mechanism of peroxymonosulfate based on supported cobalt phthalocyanine catalyst, *Appl. Catal. B Environ.* 154 (2014) 36–43.
- [61] Y. Gao, Z. Chen, Y. Zhu, T. Li, C. Hu, New insights into the generation of singlet oxygen in the metal-free peroxymonosulfate activation process: Important role of electron-deficient carbon atoms, *Environ. Sci. Technol.* 54 (2019) 1232–1241.
- [62] W. Ren, P. Zhou, G. Nie, C. Cheng, X. Duan, H. Zhang, S. Wang, Hydroxyl radical dominated elimination of plasticizers by peroxymonosulfate on metal-free boron: Kinetics and mechanisms, *Water Res.* 186 (2020), 116361.
- [63] N. Zhao, K. Liu, C. He, J. Gao, W. Zhang, T. Zhao, D.C. Tsang, R. Qiu, Singlet oxygen mediated the selective removal of oxytetracycline in C/Fe₃C/Fe⁰ system as compared to chloramphenicol, *Environ. Int.* 143 (2020), 105899.
- [64] T. Li, L. Ge, X. Peng, W. Wang, W. Zhang, Enhanced degradation of sulfamethoxazole by a novel Fenton-like system with significantly reduced consumption of H₂O₂ activated by g-C₃N₄/MgO composite, *Water Res.* 190 (2021), 116777.
- [65] A. Jawad, K. Zhan, H. Wang, A. Shahzad, Z. Zeng, J. Wang, X. Zhou, H. Ullah, Z. Chen, Z. Chen, Tuning of persulfate activation from a free radical to a nonradical pathway through the incorporation of non-redox magnesium oxide, *Environ. Sci. Technol.* 54 (2020) 2476–2488.
- [66] Y. Zhou, J. Jiang, Y. Gao, S.-Y. Pang, J. Ma, J. Duan, Q. Guo, J. Li, Y. Yang, Oxidation of steroid estrogens by peroxymonosulfate (PMS) and effect of bromide and chloride ions: kinetics, products, and modeling, *Water Res.* 138 (2018) 56–66.

- [67] L. Hu, A.M. Stemig, K.H. Wammer, T.J. Strathmann, Oxidation of antibiotics during water treatment with potassium permanganate: reaction pathways and deactivation, *Environ. Sci. Technol.* 45 (2011) 3635–3642.
- [68] M.M. Huber, T.A. Ternes, U. Von, Gunten, Removal of estrogenic activity and formation of oxidation products during ozonation of 17 α -ethinylestradiol, *Environ. Sci. Technol.* 38 (2004) 5177–5186.
- [69] Y. Ohko, K.-i. Iuchi, C. Niwa, T. Tatsuma, T. Nakashima, T. Iguchi, Y. Kubota, A. Fujishima, 17 β -Estradiol degradation by TiO₂ photocatalysis as a means of reducing estrogenic activity, *Environ. Sci. Technol.* 36 (2002) 4175–4181.
- [70] S. Pescatori, F. Berardinelli, J. Albanesi, P. Ascenzi, M. Marino, A. Antocchia, A. Di Masi, F. Acconcia, A tale of ice and fire: the dual role for 17 β -estradiol in balancing DNA damage and genome integrity, *Cancers* 13 (2021) 1583.
- [71] Q.-Y. Wu, Z.-F. Liang, W.-L. Wang, Y. Du, H.-Y. Hu, L.-L. Yang, W.-C. Huang, Non-volatile disinfection byproducts are far more toxic to mammalian cells than volatile byproducts, *Water Res.* 183 (2020), 116080.
- [72] H.K. Bhat, G. Calaf, T.K. Hei, T. Loya, J.V. Vadgama, Critical role of oxidative stress in estrogen-induced carcinogenesis, *Proc. Natl. Acad. Sci.* 100 (2003) 3913–3918.
- [73] T. Iso, T. Watanabe, T. Iwamoto, A. Shimamoto, Y. Furuichi, DNA damage caused by bisphenol A and estradiol through estrogenic activity, *Biol. Pharm. Bull.* 29 (2006) 206–210.
- [74] S.S. Lau, X. Wei, K. Bokenkamp, E.D. Wagner, M.J. Plewa, W.A. Mitch, Assessing additivity of cytotoxicity associated with disinfection byproducts in potable reuse and conventional drinking waters, *Environ. Sci. Technol.* 54 (2020) 5729–5736.
- [75] S.A. Ahmed, The immune system as a potential target for environmental estrogens (endocrine disruptors): a new emerging field, *Toxicology* 150 (2000) 191–206.